Electronic Supplementary Information for

Air-Stable Bismuth Sulfobromide (BiSBr) Visible-Light Absorbers: Optoelectronic Properties and Potential for Energy Harvesting

Xiaoyu Guo,[a] Yi-Teng Huang,[a] Hugh Lohan,[a] Junzhi Ye,[a] Yuanbao Lin,[a] Juhwan Lim,[b] Nicolas Gauriot,[b] Szymon J. Zelewski,[b] Daniel Darvill,[c] Huimin Zhu,[d,a] Akshay Rao,[b] Iain McCulloch,[a] and Robert L. Z. Hoye *,[a]

[a] Department of Chemistry, University of Oxford, South Parks Road, Oxford OX1 3QR, United Kingdom

[b] Cavendish Laboratory, University of Cambridge, Cambridge CB3 0HE, United Kingdom

[c] Department of Materials, Imperial College London, South Kensington Campus, London SW7

[d] Department of Physics, University of Strathclyde, Glasgow G4 0NG, United Kingdom

2AZ, United Kingdom

Email: robert.hoye@chem.ox.ac.uk

Table S1. Atomic percentage of Bi, S, Br elements in the bulk of BiSBr thin films annealed at various temperatures and durations, as measured by SEM-EDX

Annealing temperature (°C)	Duration (min)	Bi	S	Br	Bi:S:Br ratio
200	30	30.0	30.1	39.9	1.00: 1.00: 1.33
220	10	29.6	29.2	41.2	1.01: 1.00: 1.41
220	30	29.4	32.1	35.5	1.00: 1.09:1.21
250	10	31.9	32.1	36.0	1.00: 1.01:1.12
250	30	31.0	41.2	27.8	1.12: 1.48: 1.00
270	10	31.0	28.4	42.9	1.09: 1.00: 1.51

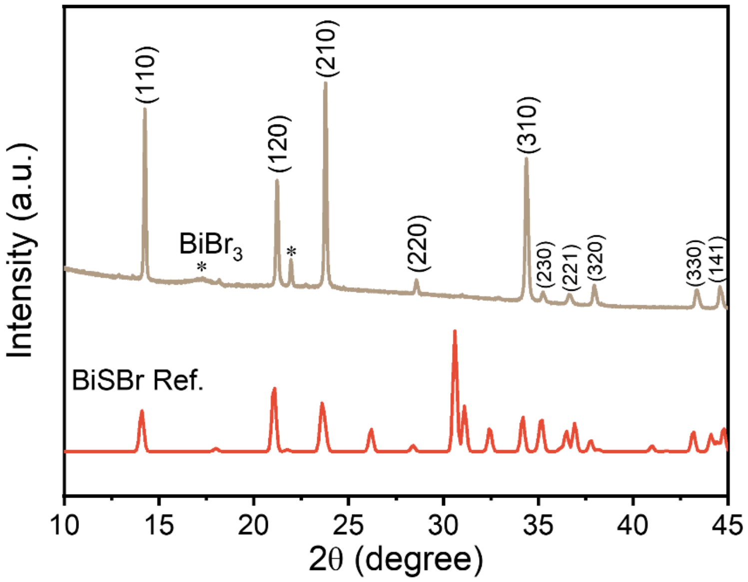

Fig. S1. XRD measurement of BiSBr thin film annealed at 270 °C for 10 min.

Table S2. Texture coefficient of BiSBr thin films annealed at various temperatures for 10 min.

Annealing temperature	2θ (°)	(hkl)	Texture coefficient	Preferred orientation
180 °C	14.1	(110)	1.42	(110)
	21.1	(120)	0.90	
	23.6	(210)	1.02	
	34.1	(310)	0.66	
200 °C	14.1	(110)	1.99	(110)
	21.1	(120)	0.66	
	23.6	(210)	0.83	
	34.1	(310)	0.53	
220 °C	14.1	(110)	1.88	(110)
	21.1	(120)	0.92	
	23.6	(210)	0.73	
	34.1	(310)	0.47	
250 °C	14.1	(110)	2.08	(110)
	21.1	(120)	0.83	
	23.6	(210)	0.70	
	34.1	(310)	0.39	
270 °C	14.1	(110)	1.66	(110)
	21.1	(120)	0.94	
	23.6	(210)	0.79	
	34.1	(310)	0.61	

In order to investigate the preferred orientation of BiSBr thin films, the texture coefficients were computed based on the XRD data. This was achieved by comparing the diffraction patterns of the films to a standard reference pattern and using Equation S1.

$$TC_{(hkl)} = \frac{\frac{I}{I_0}}{\frac{1}{N}\sum_{(hkl)}\frac{I}{I_0}} \tag{S1}$$

In Equation S1, N denotes the total number of peaks considered, I denotes the peak intensity corresponding to (hkl) in the sample's XRD pattern (normalized to the most intense peak in the whole diffraction pattern), and I_0 denotes the peak intensity of the (hkl) crystallographic plane in the standard reference pattern. We found that the preferred orientations of BiSBr thin film annealed at various temperatures (180-270 °C) for 10 min remained (110).

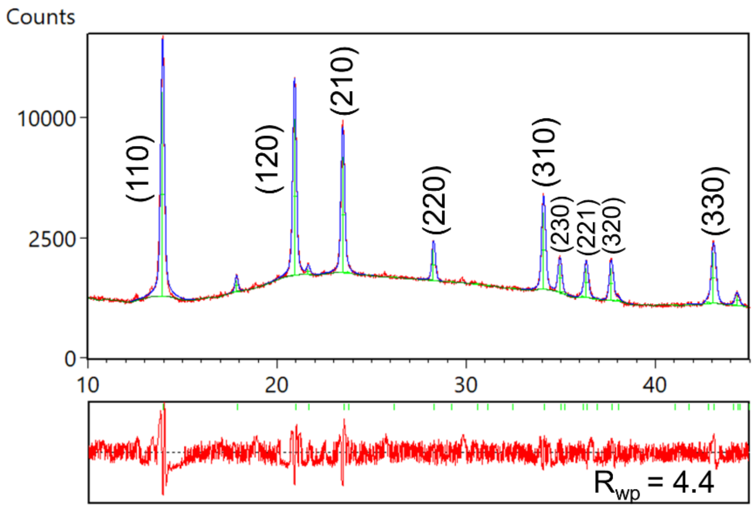

Fig. S2. XRD measurement of BiSBr thin film annealed at 250 ºC for 10 min. Pawley fitting of this data was conducted using HighScore Plus, and the R_{wp} and residuals are shown.

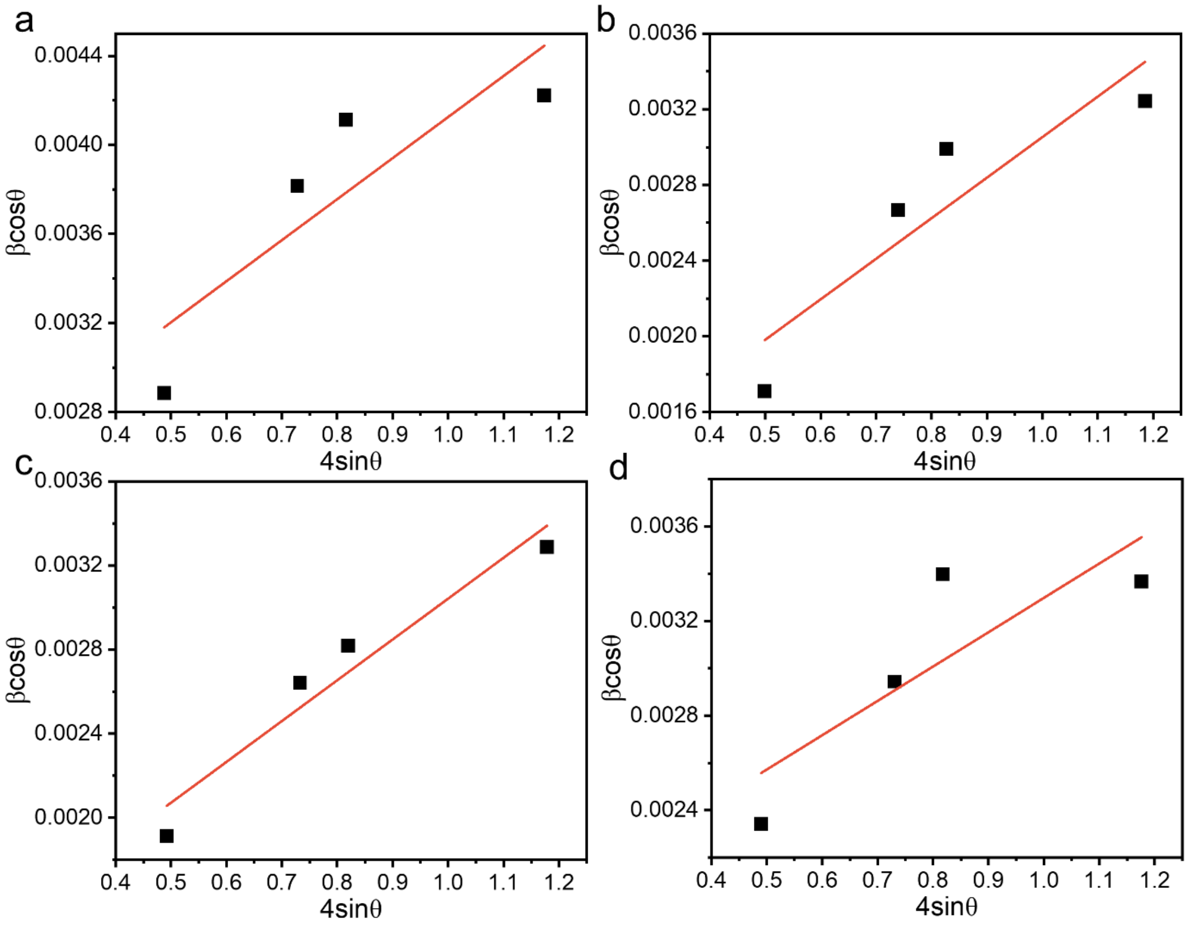

Fig. S3. Williamson-Hall plots of the diffraction patterns from BiSBr thin film annealed at (a) 200 ºC, (b) 220 ºC, (c) 250 ºC, (d) 270 ºC for 10 min in a N_2-filled glovebox.

To investigate the grain size and microstrain of thin films at various annealing temperatures according to XRD measurements, Williamson-Hall analysis is used (Equation S2). More information is available in a previous report.[1]

$$\beta\cos\theta = \left(\frac{K\lambda}{D}\right) + (4\varepsilon\, sin\theta) \tag{S2}$$

In Equation S2, *K* is the Scherrer constant. The value of *K* that is suitable for needle-like grains is 0.89.[2] λ is the X-ray wavelength, 1.5406 Å. *D* is the average size of the ordered crystalline domains, which is possibly lower than the grain size or equal to it. β (in radians) represents the line broadening at full width half maximum (FWHM), after instrument broadening has been subtracted. The instrument broadening corresponds to the breadth of the X-ray source and flat sample surface, as well as the X-ray beam's axial divergence[3] and the its value used in the calculation refers to the most recent measurement of standard LaB6 NIST660c on the Bruker.[4] ε refers to the microstrain and θ denotes the Bragg angle of the diffraction peak.

Table S3. Calculation of grain size and microstrain based on Williamson-Hall analysis.

Temperature (°C)	Grain size (nm)	Uncertainty (nm)	Microstrain $\times 10^{-3}$	Uncertainty $\times 10^{-3}$
200	61	13	1.8	0.7
220	150	45	2.1	0.7
250	124	27	1.9	0.3
270	74	22	1.4	0.7

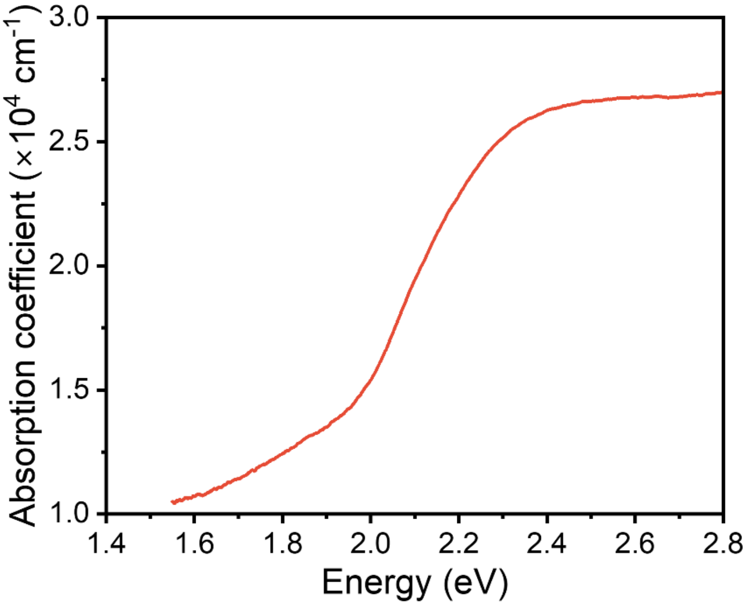

Fig. S4. Absorption coefficient spectrum of BiSBr on the quartz substrate determined from UV-Vis (transmittance and reflectance) measurements.

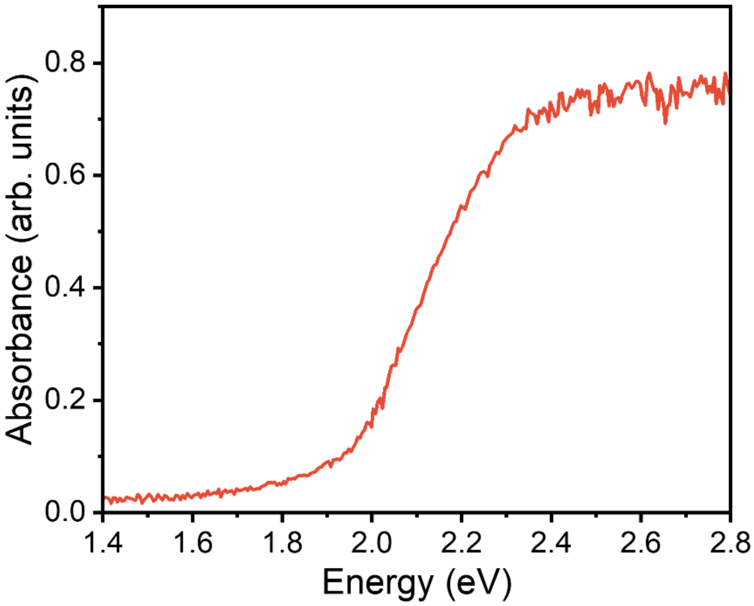

Fig. S5. Absorbance measurements of BiSBr on the quartz substrate determined from PDS measurement.

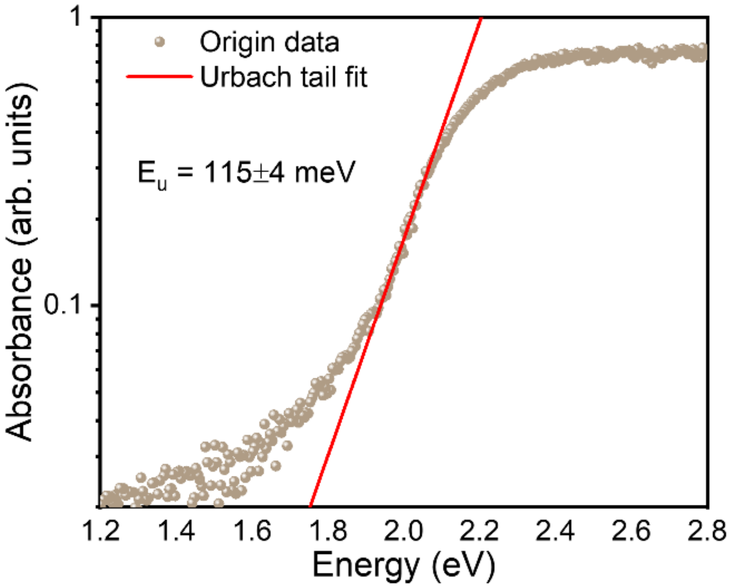

Fig. S6. Determination of the Urbach energy of BiSBr from photothermal deflection spectroscopy measurements.

The Urbach energy, U_0, can be estimated by fitting the absorption edge to an exponential function, as described by the Equation S3[5]:

$$\alpha(\mathrm{hv}) = \alpha_0 \exp\left(\frac{hv - E_g}{U_0}\right) \tag{S3}$$

In Equation S3, hv is the photon energy, E_g the bandgap, and α_0 the pre-exponential constant that describes the absorbance at the bandgap. We obtained U_0 by plotting absorbance against hv on a log-linear scale, and fitting a tangent to the absorption edge, as shown in Figure S6. The Urbach energy is then the inverse of the slope of this tangent, and we obtained a value of 115 ± 4 meV. Compared with bulk 3D lead-halide perovskite films (with typical Urbach energies in the range of 18 to 65 meV[6]), the Urbach energy of BiSBr may be higher due to a higher level of disorder or stronger carrier-phonon coupling.[7, 8] At the same time, the Urbach energy of BiSBr is at a similar level compared to other, more mature, one-dimensional semiconductors, such as Sb_2S_3 (Urbach energies100-312 meV[9, 10]) and Sb_2Se_3 (Urbach energies 71-93 meV[11]).

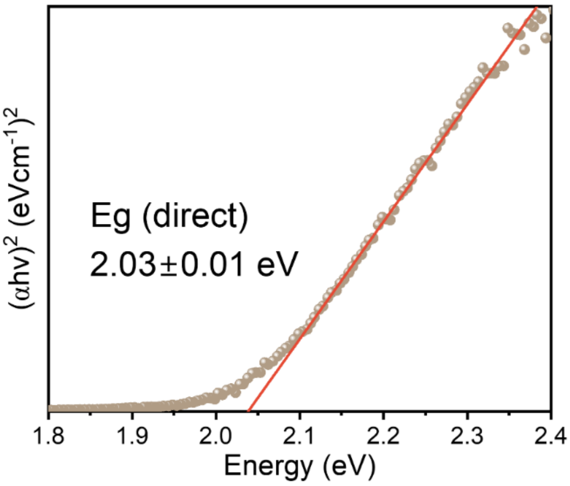

Fig. S7. Tauc plot from PDS measurement for direct bandgap estimation.

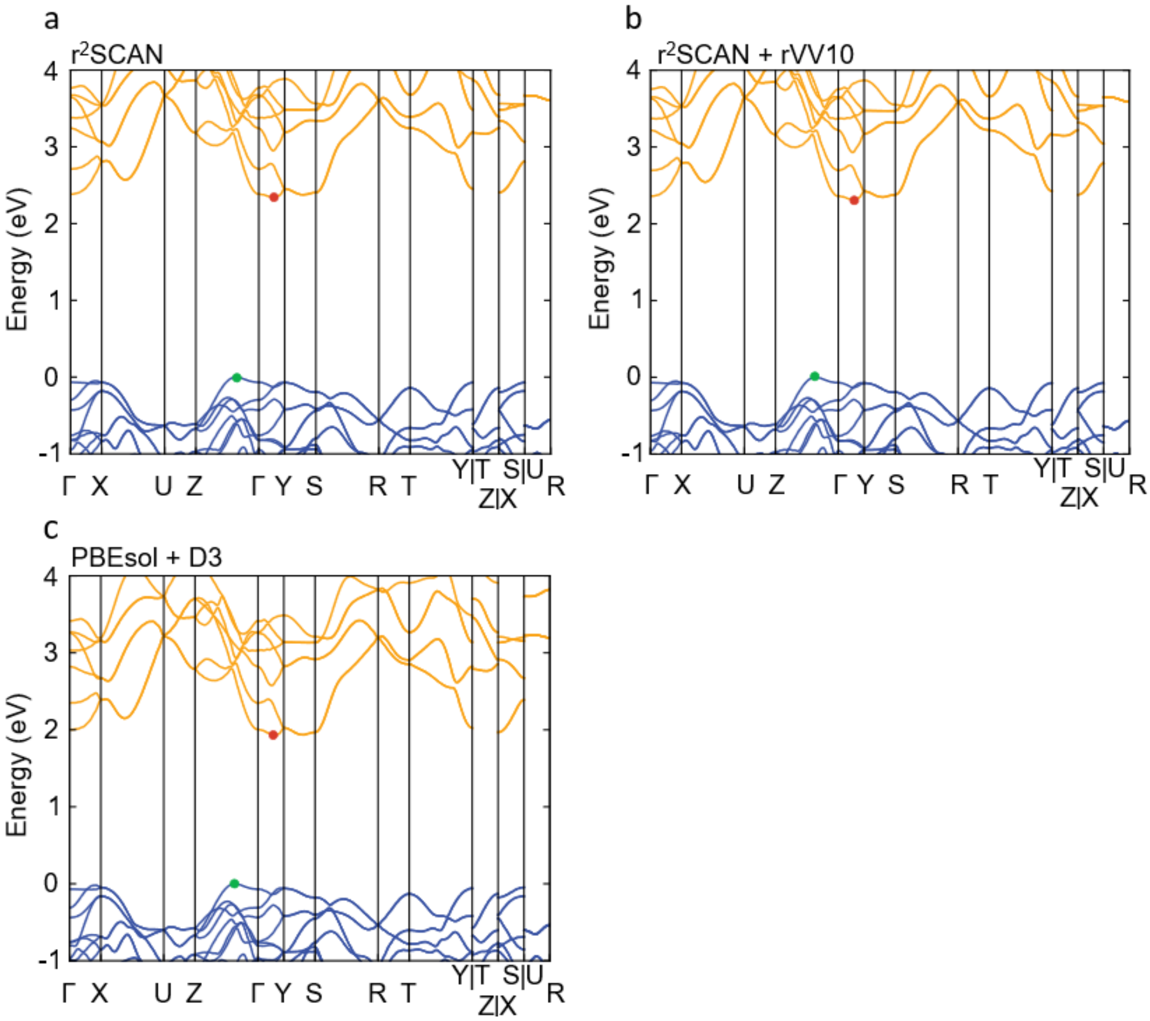

Fig. S8. Comparison of BiSBr band structures calculated using (a) pure DFT (r^{2}SCAN); (b) a *van der Waals* functional (r^{2}SCAN+rVV10); and (c) a dispersion corrected functional (PBEsol+D3). A shift in bandgap is observed between (a), (b) and (c), however the overall structures remain comparable.

The electronic structure of BiSBr has been probed at high levels of theory (HSE06+SOC[12, 13], G_0W_0+BSE@HSE06+SOC[13]), however in some cases a direct band edge is predicted in contrast to experiment. Here, we aimed to probe to effect of the *van der Waals* correction on direct/indirect gap prediction by comparing the band structures of *van der Waals* corrected and uncorrected (meta-)GGA functionals. Using a fixed structure (ICSD 31389), the revised GGA functional of Perdew, Burke, and Ernzerhof for solids (PBEsol)[14] in conjunction with the D3 dispersion correction of Grimme *et. al.*,[15, 16] and the r^2SCAN+rVV10[17] *van der Waals* functional were compared to a pure r^2SCAN band structure. We found minimal change in the nature of the band edge (*i.e.*, all indirect and at comparable **k**-points), with the primary difference being predicted band gaps.

Table S4. Experimental and DFT lattice parameters for BiSBr. Units: Å in all cases

	Theory	Exp. (refers to ICSD Coll. Code 31389)
a	8.3462	8.1666
b	10.1347	9.8532
c	4.0729	4.0492

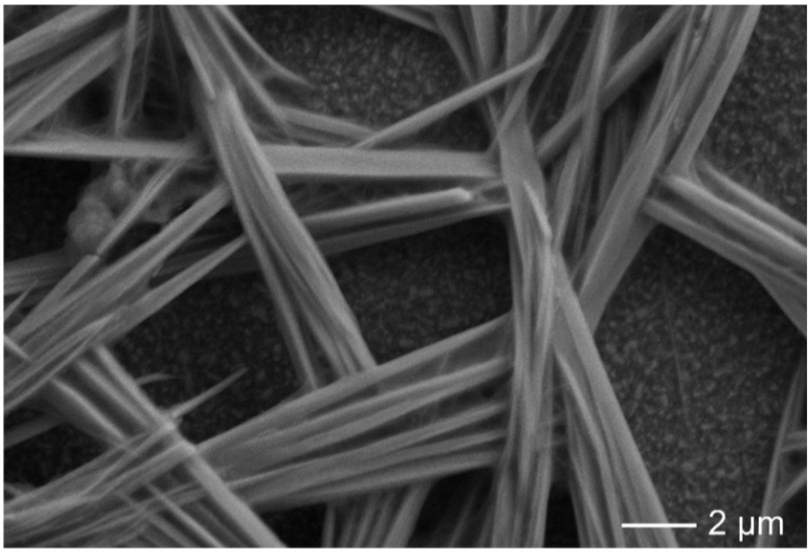

Fig. S9. High-resolution scanning electron microscopy (SEM) image of BiSBr thin film.

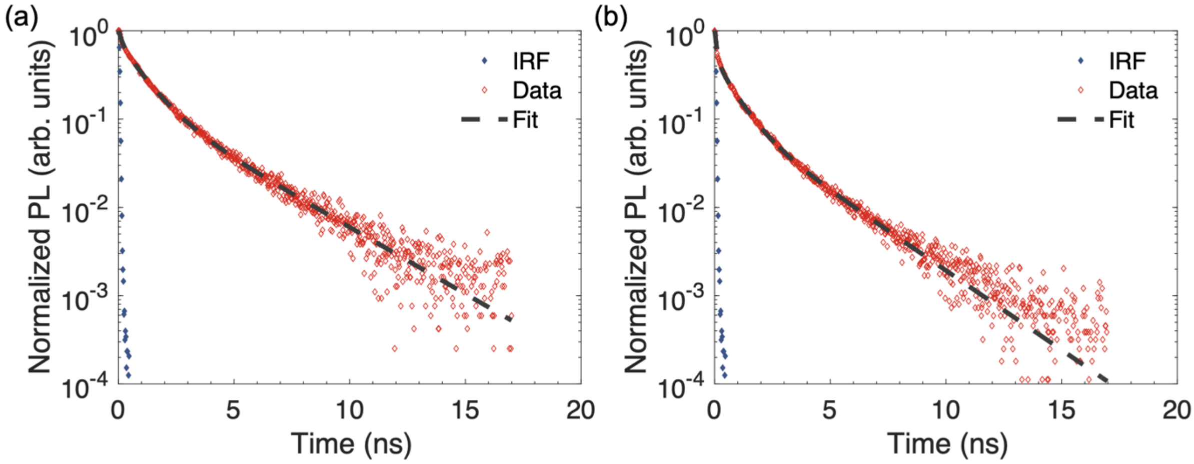

Fig. S10. Comparison of the measured PL decays of BiSBr at 10.9 µW and 56.9 µW excitation laser power with the instrument response function (IRF) and tri-exponential model fit.

Table S5. Parameters fit to the photoluminescence (PL) decays measured from BiSBr thin films using a confocal microscope. The excitation wavelength was 520 nm, which was pulsed with a repetition rate of 5 MHz (see Experimental Section in the main text for details). A phenomenological tri-exponential model was fit here, where the normalized PL intensity, I, is modelled by $I = A_1 \exp(-t/\tau_1) + A_2 \exp(-t/\tau_2) + A_3 \exp(-t/\tau_3)$. And the average lifetime is calculated using the formula: $\tau_{average} = (A_1 \times \tau_1^2 + A_2 \times \tau_2^2 + A_3 \times \tau_3^2) / (A_1 \times \tau_1 + A_2 \times \tau_2 + A_3 \times \tau_3)$.

Parameter/power (µW)	**10.9**	**56.9**
A_1	0.19	0.12
τ_1 (ns)	2.88	2.41
A_2	0.57	0.36
τ_2 (ns)	0.94	0.77
A_3	0.29	0.58
τ_3 (ns)	0.14	0.09
$\tau_{average}$ (ns)	1.86	1.48

Table S6. Parameters used to fit the PL decay of BiSBr with a model developed based on drift-diffusion equations, as described in detail in Ref. [18] and [19]. A comparison between the fits obtained from this model with the measured PL decay curves are shown in Fig. 3b of the main text. Please note that we could not directly measure the spot size of the laser in the confocal microscope, but we estimate it to be close to the diffraction limit, with a diameter of approximately 300 nm. We found that regardless of what the spot size of the laser was, we obtained very similar overall effective lifetimes from this fitting model. That is, the average excess carrier density was adjusted during fitting, such that the overall lifetime obtained was the same.

Parameter	**Excitation laser power (μW)**	
	10.9	**56.9**
Used for fitting		
Fitting window (ns)	0–17	
Background carrier concentration (cm^{-3})*	2.5×10^{9}	
Wavelength (nm)	520	
Absorption coefficient at 520 nm wavelength (cm^{-1})	2.6×10^{4}	
Reflectance at 520 nm wavelength	0.11	
Film thickness (nm)	240	
Repetition rate (MHz)	5	
Spot diameter (μm)	0.3	
Obtained from fitting		
k_1 (s^{-1})	9.96×10^{7}	9.95×10^{6}
k_2 (s^{-1} cm^{-3})	2.38×10^{-9}	1.43×10^{-9}
k_3 (s^{-1} cm^{-6})	1×10^{-27}	1×10^{-26}
Surface recombination velocity (cm s^{-1})	300	300
Diffusion coefficient (cm^2 s^{-1})**	0.20	0.21
Average excess carrier concentration (cm^{-3})	3.6×10^{16}	1.2×10^{17}
Effective bulk lifetime (ns)	5.3	3.1
Surface lifetime (ns)	40.5	40.5
Effective total lifetime (ns)	4.7	2.9

* Estimated from valence band to Fermi level offset measured from X-ray photoemission spectroscopy measurements

** A diffusivity of ~0.2 cm^2 s^{-1} implies a mobility of ~8 cm^2 V^{-1} s^{-1} (assuming the Einstein relation to hold), and a diffusion length of ~300 nm.

Reference

1. A. K. Zak, W. A. Majid, M. E. Abrishami and R. Yousefi, *Solid State Sciences*, 2011, **13**, 251-256.
2. J. I. Langford and A. Wilson, *Journal of Applied Crystallography*, 1978, **11**, 102-113.
3. D. Balzar, *Journal of research of the National Institute of Standards and Technology*, 1993, **98**, 321.
4. D. R. Black, M. H. Mendenhall, C. M. Brown, A. Henins, J. Filliben and J. P. Cline, *Powder Diffraction*, 2020, **35**, 17-22.
5. R. Boughalmi, A. Boukhachem, M. Kahlaoui, H. Maghraoui and M. Amlouk, *Materials Science in Semiconductor Processing*, 2014, **26**, 593-602.
6. B. Subedi, C. Li, C. Chen, D. Liu, M. M. Junda, Z. Song, Y. Yan and N. J. Podraza, *ACS Applied Materials & Interfaces*, 2022, **14**, 7796-7804.
7. R. A. Jagt, I. Bravić, L. Eyre, K. Gałkowski, J. Borowiec, K. R. Dudipala, M. Baranowski, M. Dyksik, T. W. van de Goor, T. Kreouzis, M. Xiao, A. Bevan, P. Płochocka, S. D. Stranks, F. Deschler, B. Monserrat, J. L. MacManus-Driscoll, R. L. Z. Hoye, *Nature Communications*, 2023, **14**, 2452.
8. S. R. Rondiya, R. A. Jagt, J. L. MacManus-Driscoll, A. Walsh and R. L. Hoye, *Applied Physics Letters*, 2021, **119**.
9. R. S. Marquina, T. Sanchez, N. Mathews and X. Mathew, *Materials Research Bulletin*, 2017, **90**, 285-294.
10. M. H. Lakhdar, B. Ouni and M. Amlouk, *Optik*, 2014, **125**, 2295-2301.
11. S. Ghosh, M. Moreira, C. Fantini and J. González, *Solar Energy*, 2020, **211**, 613-621.
12. Z. Ran, X. Wang, Y. Li, D. Yang, X.-G. Zhao, K. Biswas, D. J. Singh and L. Zhang, *npj Computational Materials*, 2018, **4**, 14.
13. J. M. Booth, M. V. Klymenko, J. H. Cole and S. P. Russo, *Physical Review B*, 2021, **103**, 115203.
14. J. P. Perdew, A. Ruzsinszky, G. I. Csonka, O. A. Vydrov, G. E. Scuseria, L. A. Constantin, X. Zhou and K. Burke, *Physical Review Letters*, 2008, **100**, 136406.
15. S. Grimme, J. Antony, S. Ehrlich and H. Krieg, *The Journal of Chemical Physics*, 2010, **132**.
16. S. Grimme, S. Ehrlich and L. Goerigk, *Journal of Computational Chemistry*, 2011, **32**, 1456-1465.
17. J. Ning, M. Kothakonda, J. W. Furness, A. D. Kaplan, S. Ehlert, J. G. Brandenburg, J. P. Perdew and J. Sun, *Physical Review B*, 2022, **106**, 075422.
18. J. R. Poindexter, R. L. Z. Hoye, L. Nienhaus, R. C. Kurchin, A. E. Morishige, E. E. Looney, A. Osherov, J.-P. Correa-Baena, B. Lai and V. Bulović, V. Stevanović, M. G. Bawendi, T. Buonassisi, *ACS Nano*, 2017, **11**, 7101-7109.
19. R. L. Z. Hoye, L. C. Lee, R. C. Kurchin, T. N. Huq, K. H. L. Zhang, M. Sponseller, L. Nienhaus, R. E. Brandt, J. Jean J. A. Polizzotti, A. Kursumović, M. G. Bawendi, V. Bulović, V. Stevanović, T. Buonassisi, J. L. MacManus-Driscoll, *Advanced Materials*, 2017, **29**, 1702176.